Supporting Information

Rationally Designed Porous Self-Assembled Nanoparticles for Combinational Chemo-Photodynamic Therapy

Kanchan Negi[a], Ashok Kumar[a], Gourav Chakraborty[a], Sudhansubala Sahoo[a], Sushmita Patra[b], Niladri Patra[a], Sujit Kumar Bhutia[b] and Sumanta Kumar Sahu[a*]

[a] Department of Chemistry and Chemical Biology, Indian Institute of Technology (ISM), Dhanbad 826004, Jharkhand, India.

[b]Department of Life Science, National Institute of Technology Rourkela, 769008, Odisha, India.

* Corresponding author. E-mail: sumantchem@gmail.com, sksahu@iitism.ac.in;
Tel: +91 3262235936, +91 7631042241

---

1. Materials and Reagents Used

2,2,6,6-tetramethylpiperidine (TEMP, 98%) and Quercetin hydrate ($C_{15}H_{10}O_7.H_2O$, 96 %) were bought from TCI Co., Ltd. Ethanol (EtOH) and Zinc acetate dihydrate ($Zn(CH_3COO)_2.2H_2O$, 98 %) was obtained from Merck. 1,3-diphenyl-isobenzofuran (DPBF), and 3-(4,5-Dimethylthiazol-2-yl)-2,5-diphenyltetrazolium bromide (MTT) was acquired from Sigma Aldrich. Dimethyl formamide was bought from Rankem, India Ltd. Chlorin e6 (Ce6) was purchased from BLD Pharmatech (India) Pvt. Ltd. 2',7'-dichlorofluorescein 3',6'-diacetate (DCFH-DA) was obtained from Thermofisher Scientific. Calcein AM and EthD-III were bought from Biotium. Fetal bovine serum (FBS), Dulbecco's Modified Eagle's Medium (DMEM), Poly-D-Lysine, Phosphate buffered saline (PBS), and Fluoromount G were purchased from Gibco New York. The entire experiment was carried out with Millipore water. All the chemicals were of analytical grade and were used without any further processing.

2. Characterizations

The morphological information and size distribution were analyzed using a Supra 55, Carl Zeiss Field emission scanning electron microscope, and Talos F200X G2 high-resolution transmission electron microscope (HRTEM). A UV-vis spectrophotometer (Shimadzu, UV-2600, Japan) was employed to acquire the UV-visible absorption spectra. An Agilent Cary 660 instrument was used to obtain Fourier Transform Infrared (FTIR) spectra using a KBr pellet. The high-resolution XRD patterns were collected on Rigaku Smartlab using a Cu Kα X-Ray source having wavelength 1.5406 Å within the 2θ range of 10-50°. XPS (X-ray photoemission spectroscopy) was performed on PHI, 5000 versa probe III to examine the surface functional groups. The BET surface area of NMOFs was determined by measuring the N_2 adsorption and desorption isotherms using a Gas Sorption Analyzer (Micromeritics Instrument Corporation, USA, 3FLEX 3500). TGA-DTA was performed on Perkin Elmer (STA6000) instrument, under a continuous N_2 flow rate of 50 ml/min and a temperature rise of 20 °C/min. Zeta potential and Dynamic Light Scattering measurements were quantified using zetasizer Nano ZS (Malvern, UK). The irradiating source was a 635 nm laser (RLM650TB-030FC, Shanghai Laser & Optics Century Co., Ltd. (SLOC))**.** Intracellular fluorescence images were acquired using a Leica DMi8 epi-fluorescence microscope. BD ACCURI C6 Flow Cytometer was used to analyze the cell death mechanism.

3. Molecular Dynamics (MD) Simulations:

MD simulations were carried out to determine the nature of interactions between the Ce6 moiety with ZnQ self-assembly. The simulations were performed using GROMACS 2021.2 (MPI Version) software package. [1] The modelling of Quercetin, DMF, Ethanol, Chlorin e6, and Acetate ions was done using GAFF [2], with their respective resp charges derived from the default AM1-BCC method [3], using Antechamber [4] package of Ambertools23. [5] For Zn^{2+} ions, the parameters developed by Pengfei *et al*. were used. [6] Initially, 9 Zn^{2+} ions and 10 Quercetin molecules were randomly placed inside a 4.7 x 4.7 x 4.7 nm^3 simulation box,

replicating their experimental ratio of 87:100. This was followed by adding 18 acetate ions for neutralization and 1 Ce6 molecule. Finally, 97 DMF and 582 Ethanol molecules were packed inside the box, maintaining the experimental solvent ratio of 1:6. The packing of all the components was done using Packmol. [7] A series of minimizations using a combination of steepest descent and conjugate gradient [8,9] was performed until convergence to a maximum force of 100 kJ/(mol nm). This was followed by 150 ns of NVT equilibration, coupled with V-rescale thermostat [10], with reference temperatures fluctuating periodically between 298 K and 350 K, using simulated annealing protocol. [11] This ensured the randomization of the initial state by raising the thermal energy of system, increasing the possibility of coalescing into a more favourable clustered state, rather than getting trapped inside a local minimum. A 100 ns NPT run, with reference pressure maintained at 1 bar using Berendsen barostat, [12] and temperatures fluctuating periodically between 350K and 298 K was performed. Finally, another round of 50 ns NPT run at 298 K and 1 bar pressure was performed to relax the system under experimental conditions, followed by 250 ns of production run. During production run, the energy groups between all residue names were defined in order to calculate the pairwise interaction energies between them. In all the simulations, non-bonded cut-off for both van der Waals and electrostatic forces were set to 1.2 nm. The long-range electrostatic forces were calculated using Particle Mesh Ewald (PME) summation method [13], using an interpolation order of 6. The internal degrees of freedom for all the H-bonds were constrained using LINCS [14] algorithm. Finally, the integration step was set to 2fs.

4. Results of MD Simulations:

The temporal variation of all the plausible interaction energies between ZnQ NPs and Ce6 is shown in **Fig. S13a**. The figure shows a running average (with 15 data points) of the Coulombic, and Lennard-Jones (L-J) energies of the system during its 250 ns production length. As shown, significant contributions arise from the L-J term, with an average value of -

35.05 kJ/mol. On the other hand, Coulombic contributions are considerably lower, bearing an average of -14.98 kJ/mol. Around 90 ns, the Coulombic contribution significantly decreases, attaining a positive interaction energy. Hence, it can be concluded that the entire assembly of ZnQ, and Ce6 is predominantly stabilised via van der Waals forces. As noted experimentally, the stable Coulombic forces observed during simulations contradict the negative zeta potential values of ZnQ NPs and Ce6 molecule. This could be due to the charge distribution within the molecule, which facilitates some attractive Coulombic interactions. The plausible tripartite assembly of ZnQ NPs and Ce6, as observed from MD simulations is shown in **Fig. S13b**.

5. Optimized structures of single, tetrahedral Zn^{2+} ion bound with 2 quercetin moieties

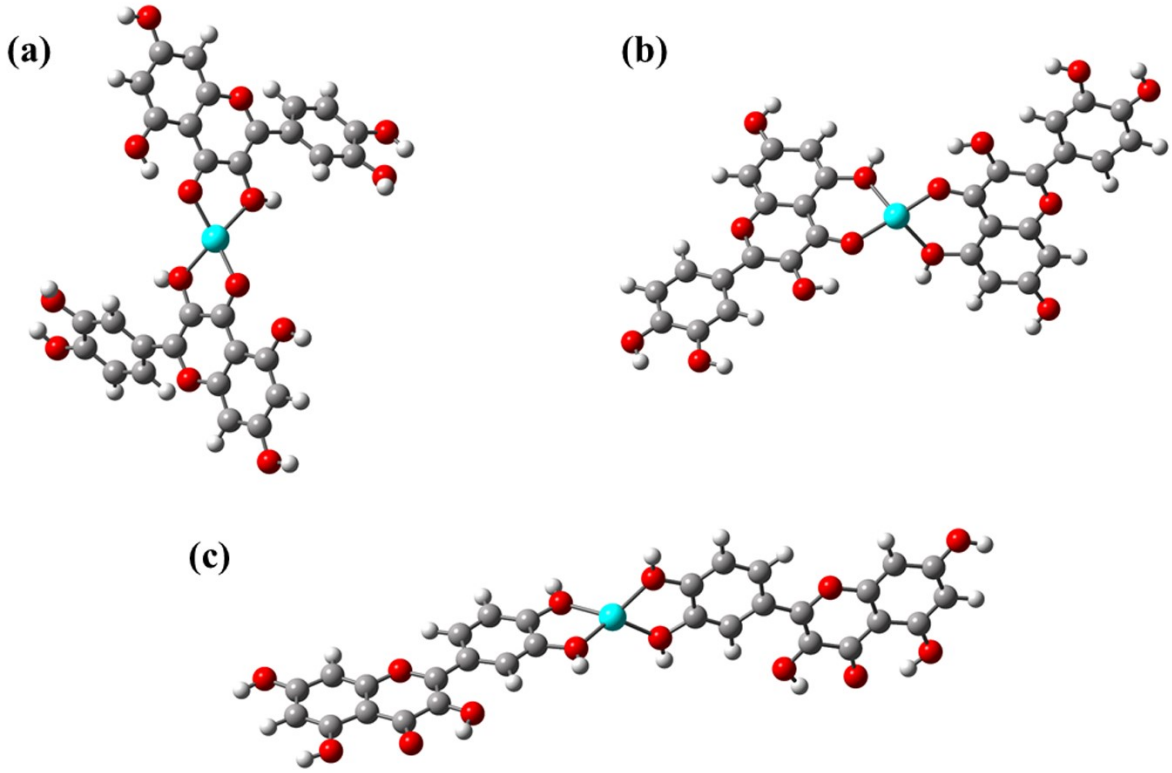

Fig. S1 Optimized structures of single, tetrahedral Zn^{2+} ion bound with 2 quercetin moieties. (a), (b), and (c) corresponding to quercetin binding via Site 1 (O3, O4), Site 2 (O4, O5), and Site 3 (O3', and O4') respectively.

6. Optimized structures of dual, tetrahedral Zn^{2+} moieties, sharing a quercetin unit

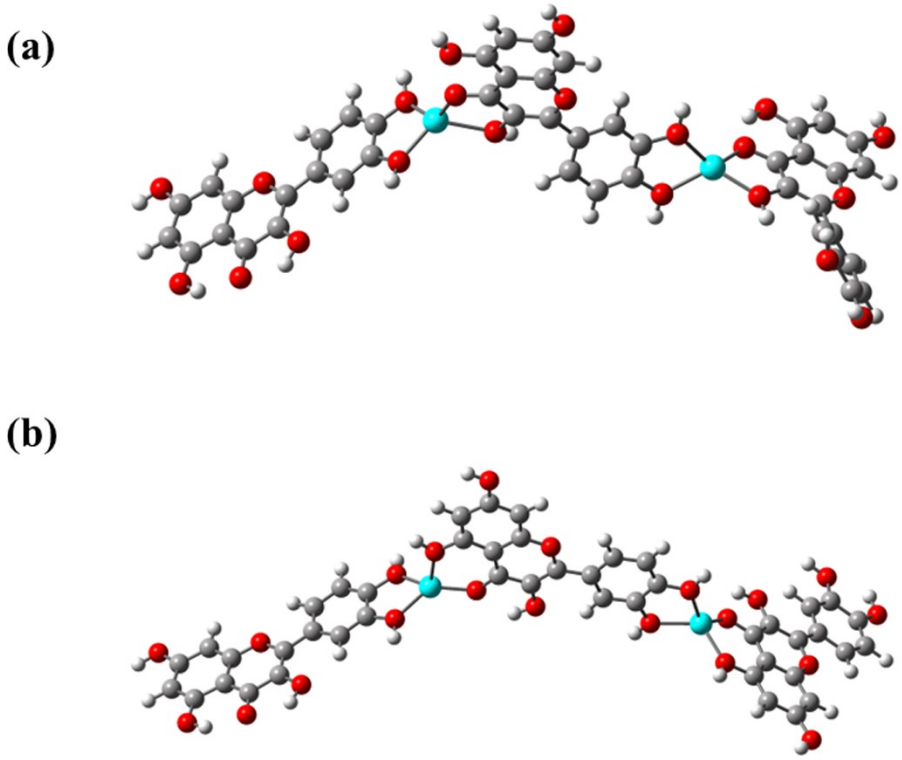

Fig. S2 Optimized structures of dual, tetrahedral Zn^{2+} moieties, sharing a quercetin unit between them. Here (a) and (b) correspond to two Site 1, and Site 2 bindings of Quercetin respectively.

7. Photographic images

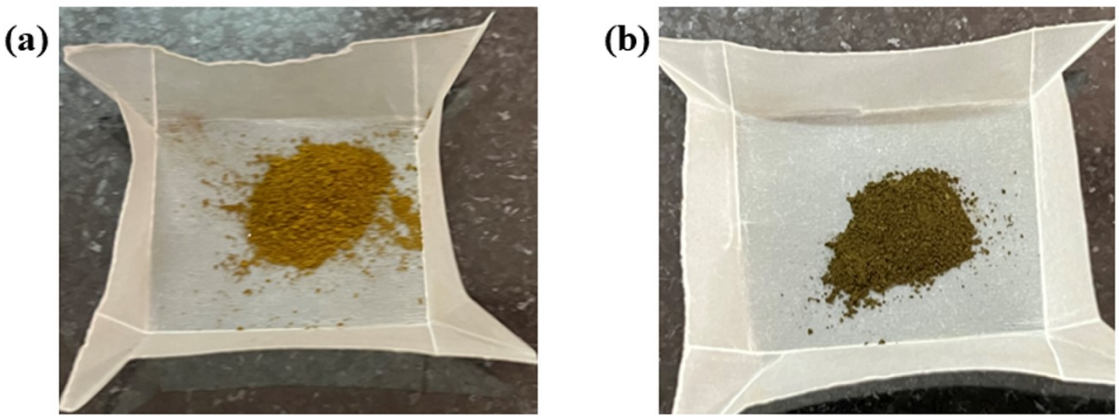

Fig. S3 Digital images of (a) ZnQ NPs and (b) ZnQ@Ce6.

8. Molecular Structure of ZnQ NPs

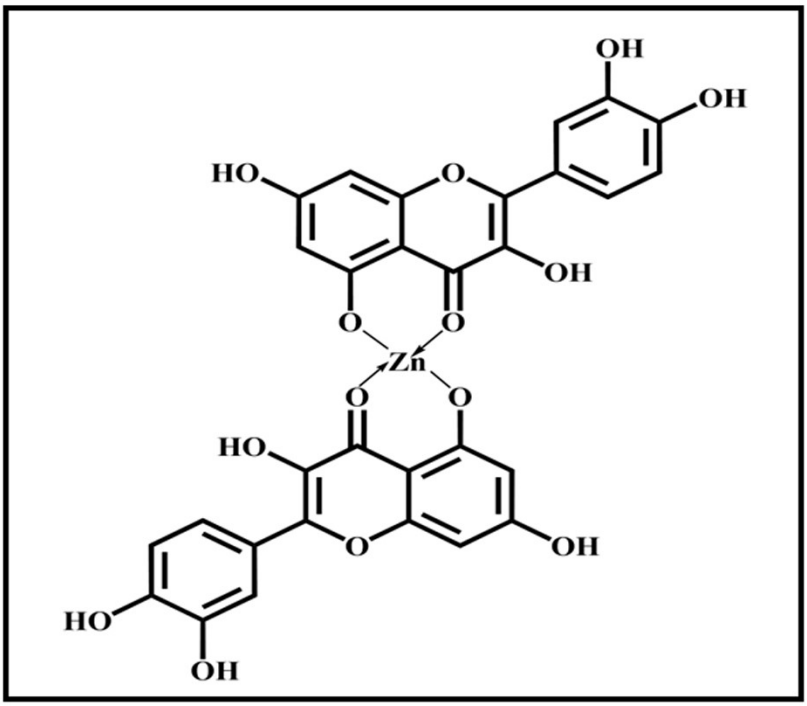

Fig. S4 Possible interaction between zinc ion and quercetin.

9. Photographic images of quercetin and ZnQ NPs solution

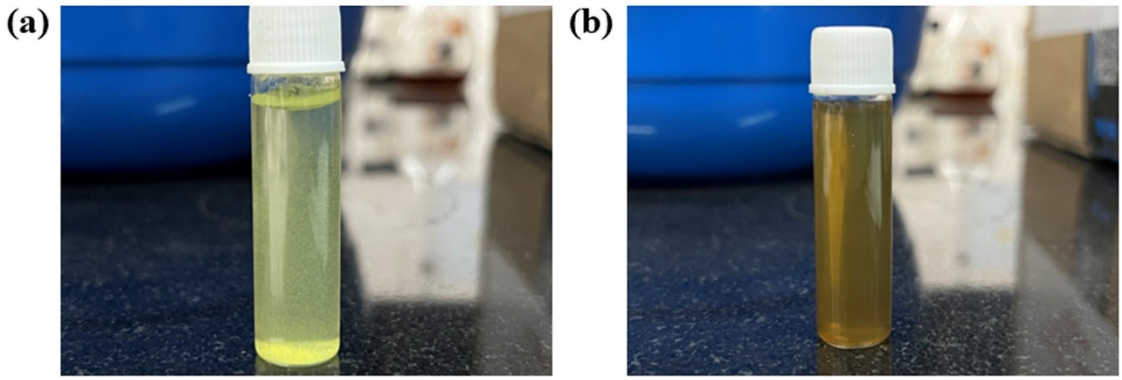

Fig. S5 Images of (a) quercetin and (b) ZnQ NPs in distilled water.

10. Elemental Mapping and EDX spectra of ZnQ NPs

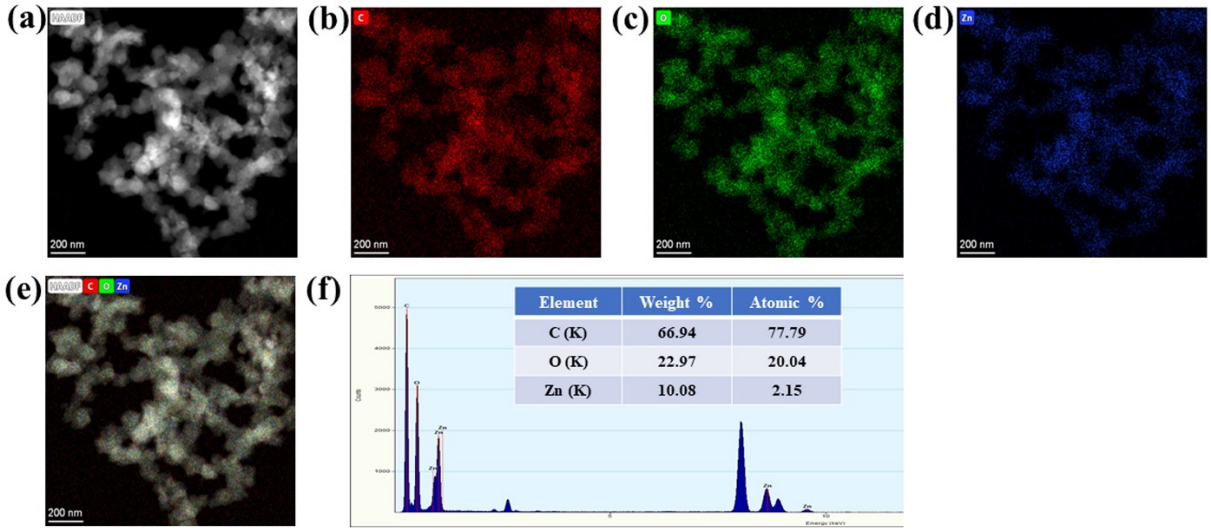

Fig. S6 Elemental mapping analysis of ZnQ NPs (a) HAADF image, (b) Carbon, (c) Oxygen, (d) Zinc, (e) Merged, and (f) EDX spectrum.

11. Elemental Mapping and EDX spectra of ZnQ@Ce6

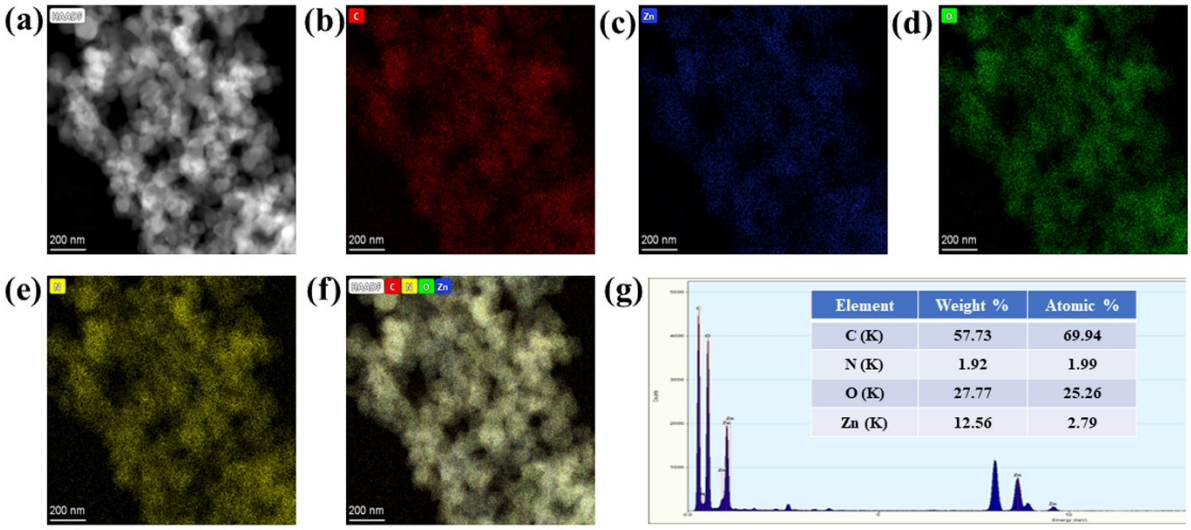

Fig. S7 Elemental mapping analysis of ZnQ@Ce6 (a) HAADF image, (b) Carbon, (c) Zinc, (d) Oxygen, (e) Nitrogen, (f) Merged, and (g) EDX spectrum.

12. SAED (Selected area electron diffraction) of ZnQ NPs

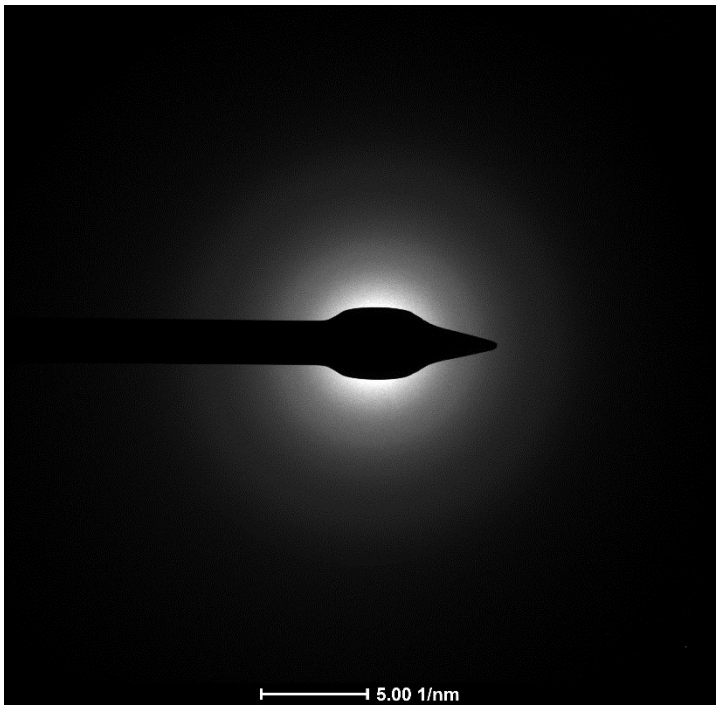

Fig. S8 SAED pattern of ZnQ NPs.

13. Stability of ZnQ NPs and ZnQ@Ce6

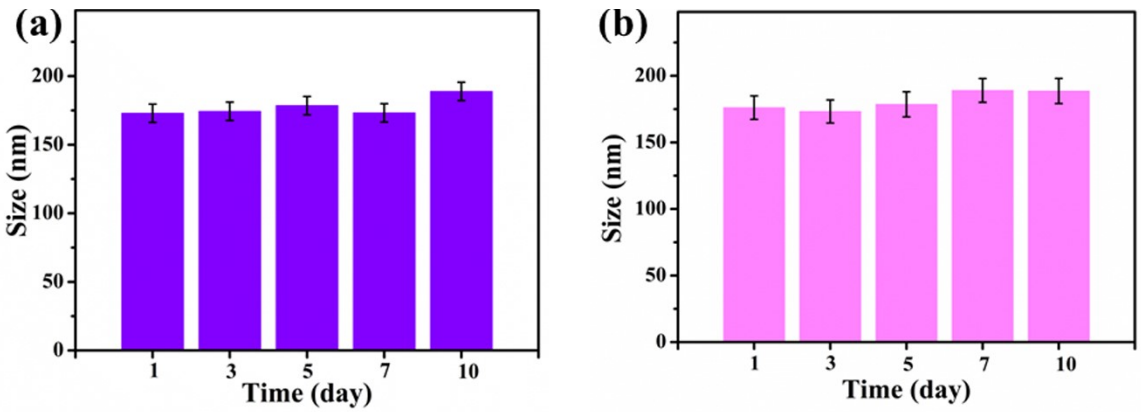

Fig. S9 The particle sizes of (a) ZnQ NPs, and (b) ZnQ@Ce6 in PBS buffer solution (pH 7.4) at a specific time.

14. XPS Analysis

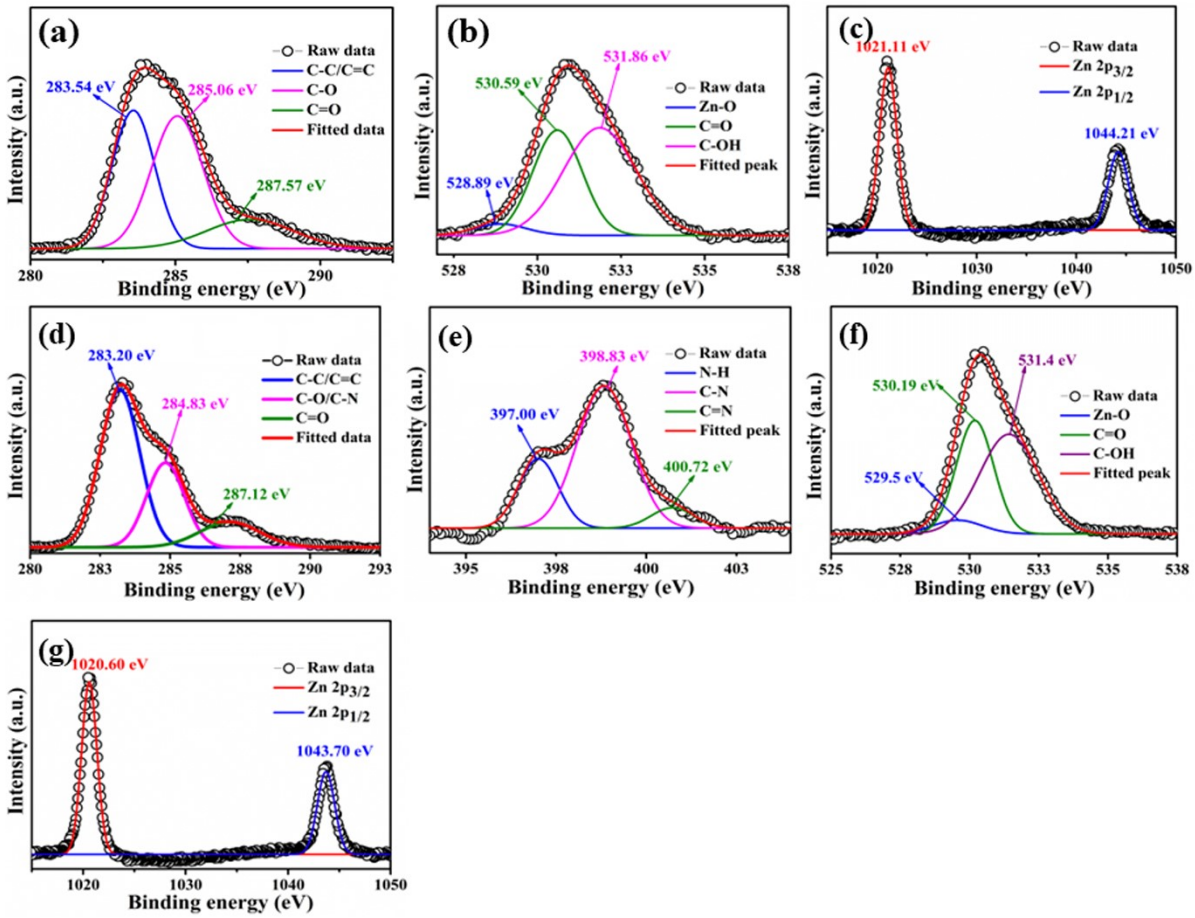

Fig. S10 HR-XPS of ZnQ NPs (a-c) and ZnQ@Ce6 (d-g).

15. BET analysis

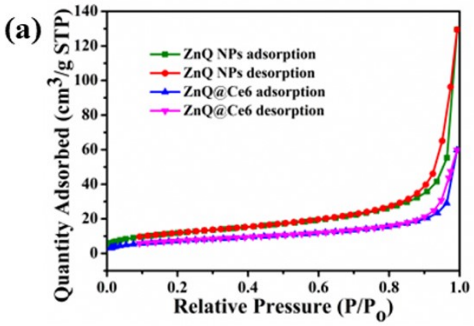

(b) BET Surface area and Pore volume

Sample Label	BET Surface Area (m^2/g)	Pore Volume (cm^3/g)
ZnQ NPs	43.0645	0.200396
ZnQ@Ce6	26.7024	0.092549

Fig. S11 (a) BET adsorption-desorption isotherm of ZnQ NPs and ZnQ@Ce6, (b) BET surface area and pore volume of ZnQ NPs, ZnQ@Ce6.

16. Absorption spectra of Chlorin e6 solution and supernatant obtained after ZnQ@Ce6 formation.

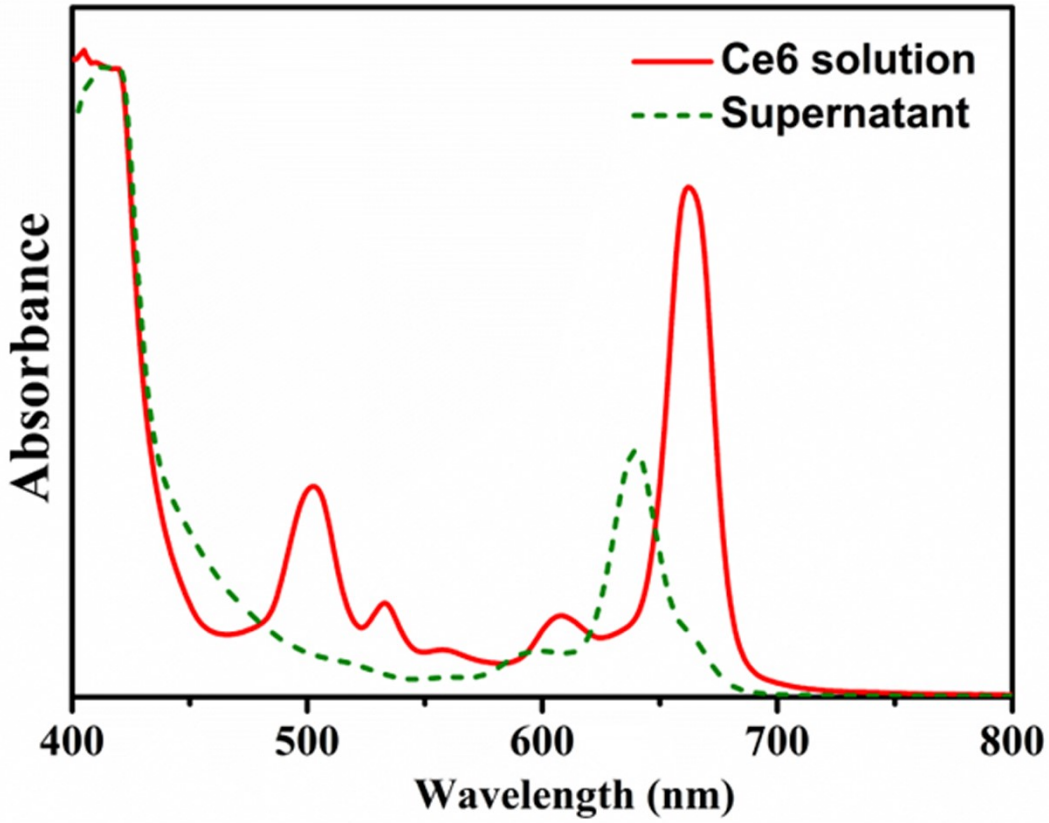

Fig. S12 Absorbance spectra of the initial Ce6 solution and the supernatant obtained after the process of ZnQ@Ce6 composite.

17. Temporal variation in Coulombic and Lennard-Jones interaction energies

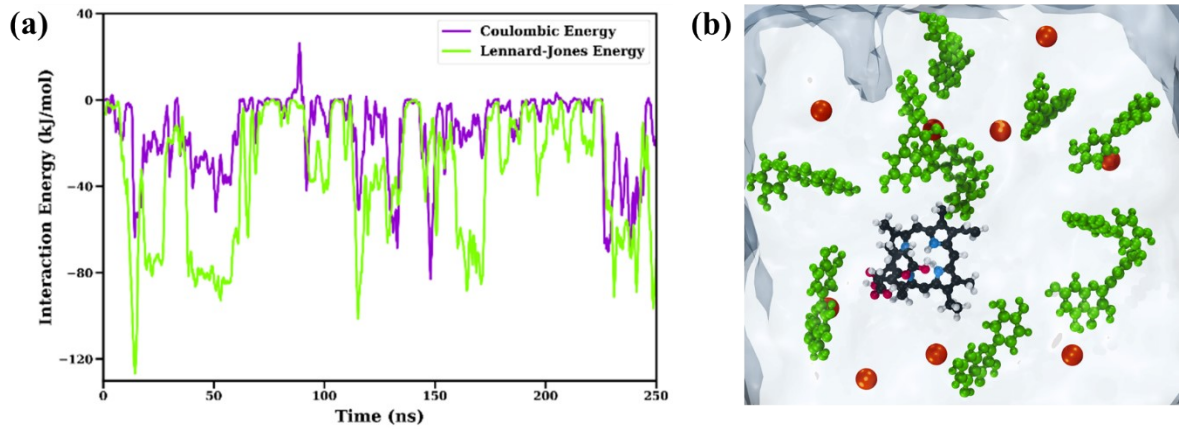

Fig. S13 (a) Temporal variation in Coulombic and Lennard-Jones interaction energies between ZnQ NPs and Chlorin e6 (Ce6), and (b) Molecular arrangement of Zn^{2+}-Quercetin-Ce6 tripartite assembly obtained from MD simulations.

18. TGA analysis

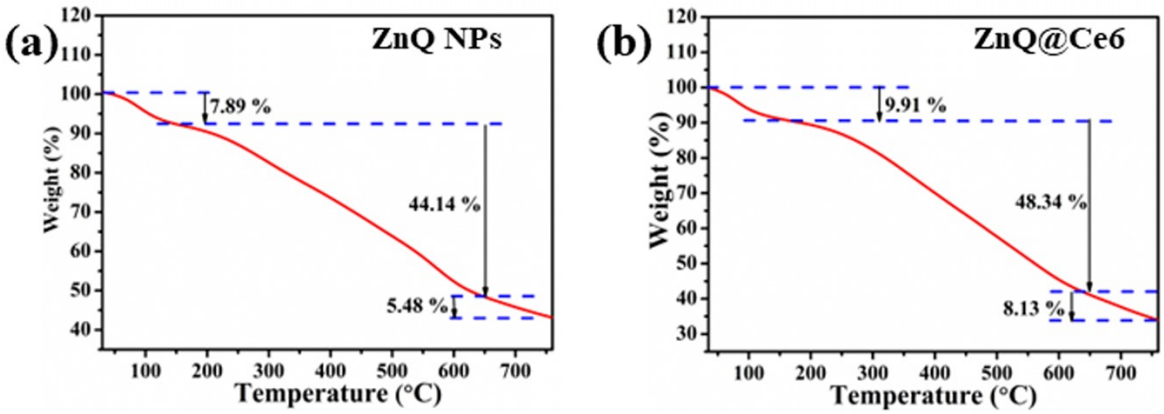

Fig. S14 TGA curve of (a) ZnQ NPs, (b) ZnQ@Ce6.

19. Calibration curve Quercetin and Chlorin e6

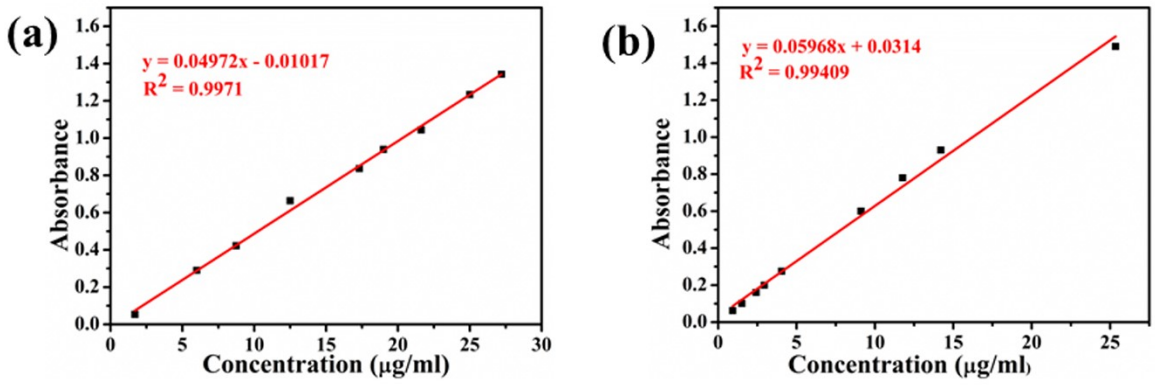

Fig. S15 (a) The standard absorbance curve of Ce6. (b) The standard absorbance curve of free quercetin.

20. Cumulative release of quercetin and Ce6 in the presence of light

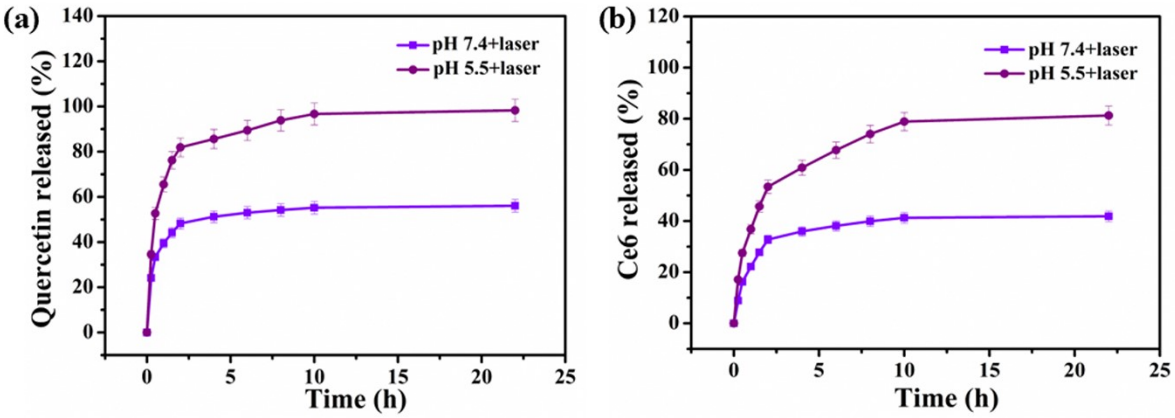

Fig. S16 Cumulative release of quercetin and Ce6 from ZnQ@Ce6 with and without laser irradiation (635nm, 60 mW/cm^2).

21. Intracellular uptake comparative study of ZnQ@Ce6 and Ce6 in HeLa cells

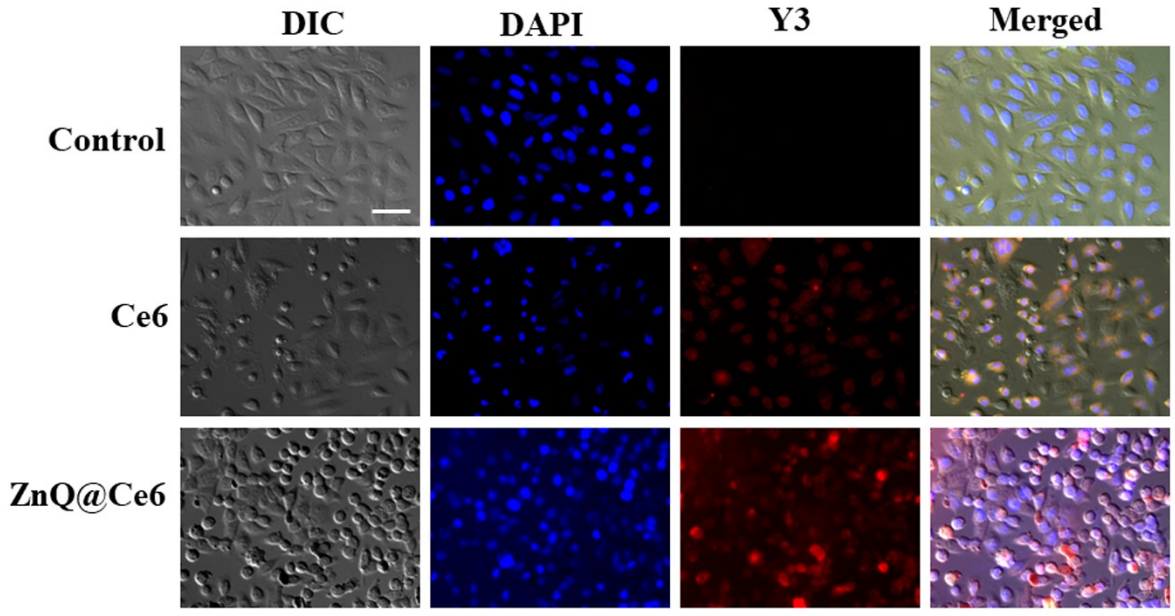

Fig. S17 Fluorescence images of HeLa cells after treatment with Ce6 and ZnQ@Ce6 for 12 h (Scale bar: 50 μm).

22. Quantitative analysis of fluorescence intensity of DCF in cells after irradiation

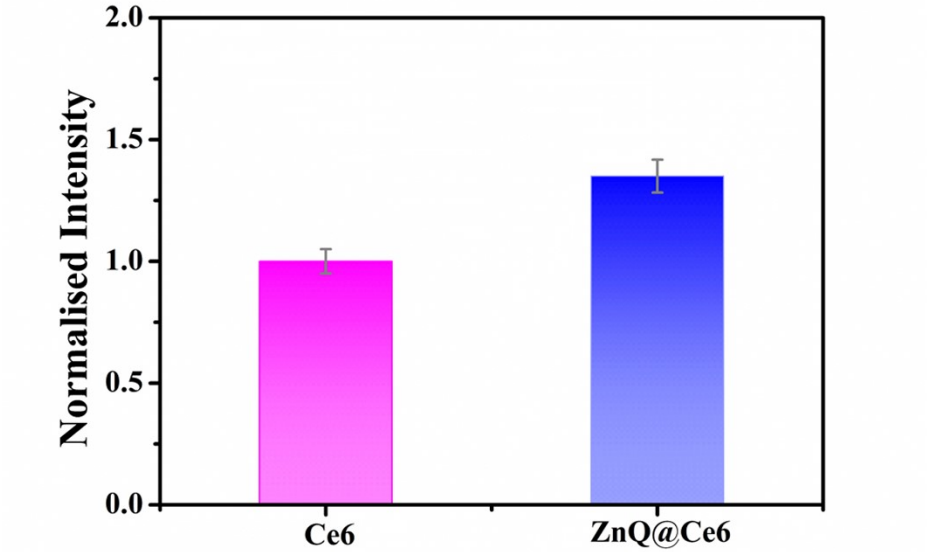

Fig. S18 The quantification of DCF fluorescence intensity from the fluorescence images of HeLa cells treated with Ce6 and ZnQ@Ce6 when exposed to a 635 nm laser.

23. Images of HeLa cells after exposure to 635 nm laser irradiation for 5 min

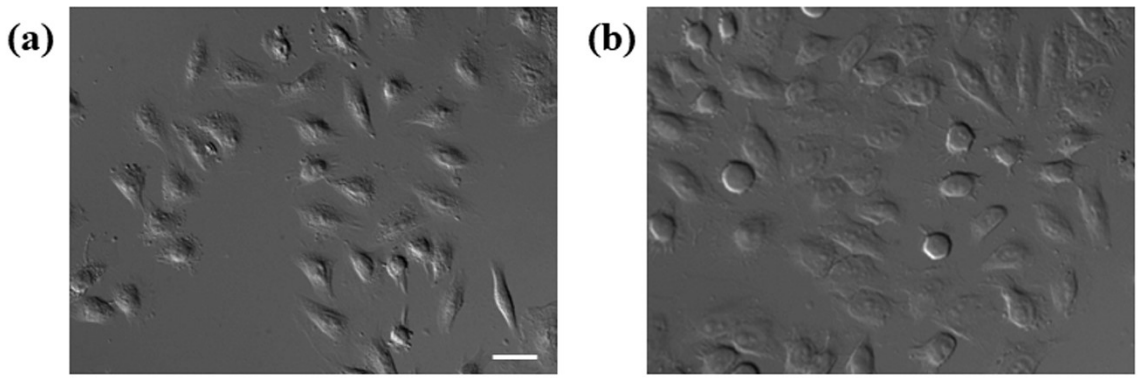

Fig. S19 *In vitro* images of HeLa cells exposed to a 635 nm laser irradiation for (a) 0 min, (b) 5 min (Scale bar: 50 μm).

24. Flow Cytometry analysis

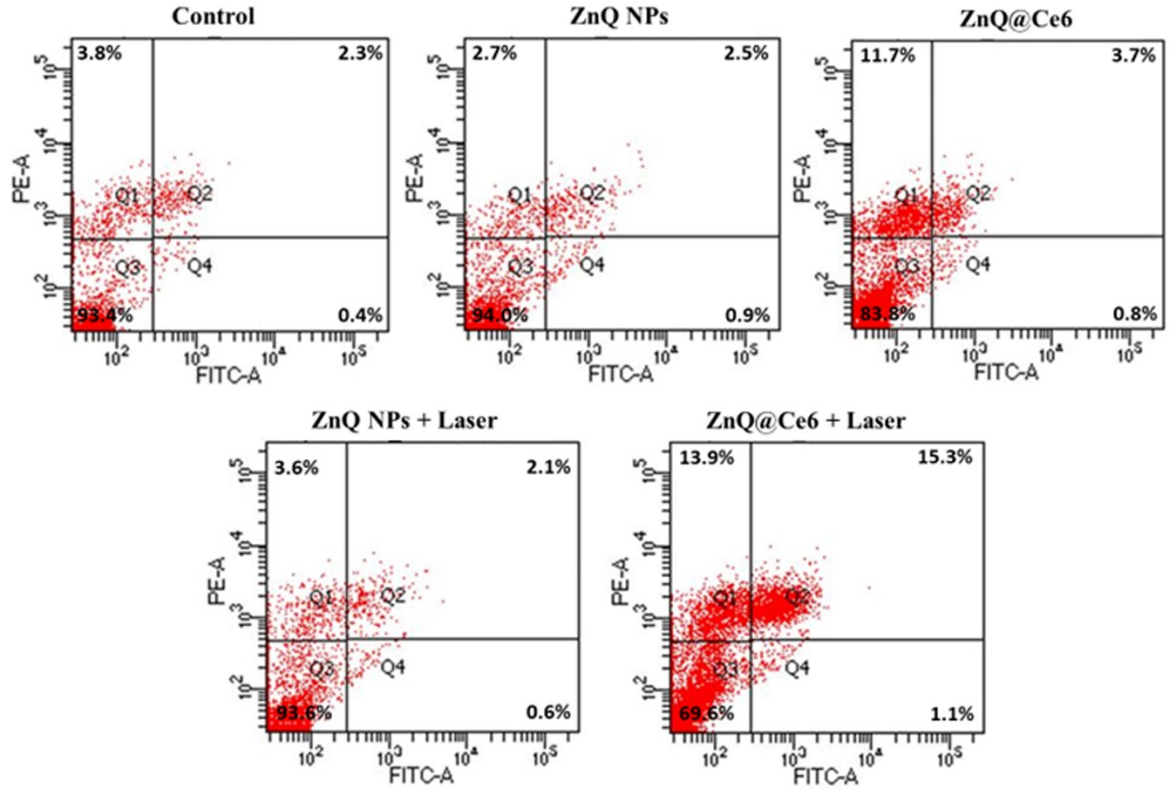

Fig. S20 HeLa cell treated with 50 µg/ml of ZnQ NPs and ZnQ@Ce6, incubated for 10 h and analyzed with Annexin V-FITC/PI staining through flow cytometry.

25. FESEM image of ZnQ@Ce6 at pH 5.5

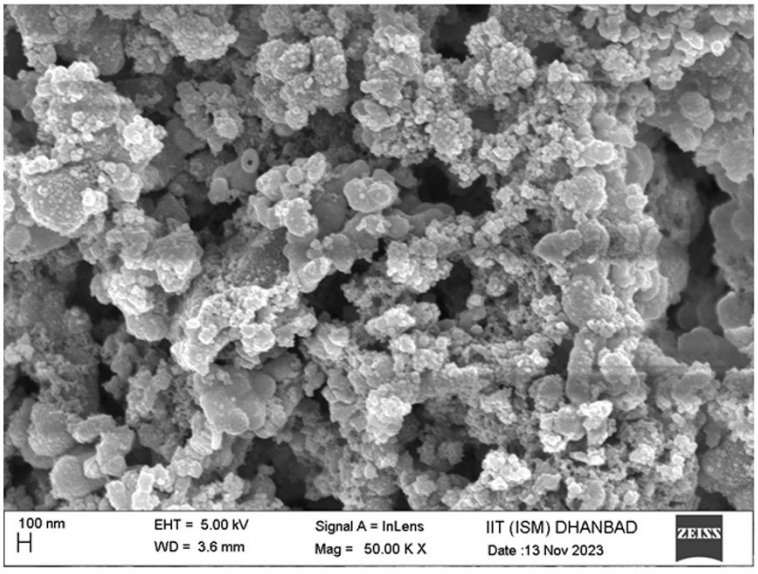

Fig. S21 FESEM image of ZnQ@Ce6 after overnight stirring at pH 5.5.

26. Comparative table of existing chemotherapeutic drugs and photodynamic therapies with this work

Nanomaterial/ nanocomposite	Chemotherapy drug	PDT agent	Loading %	Laser / Intensity	Irradiation time	Treatment method	Ref.
ZIF-8	Carbozantinib	Ce6	13.82	660 nm (80 mW/cm^2)	5 min	Multimodal antitumor therapy	15
ZIF-8	-	Ce6	11.3	660 nm (80 mW/cm^2)	10 min	Photodynamic therapy	16
Mesoporous silica NPs	Doxorubicin	ICG	6.69	808 nm (2W/cm^2)	5 min	Chemo-PDT	17
Micelles	Camptothecin	Porphyrin	6.2	650 nm (500mW/cm^2)	5 min	Chemo-PDT	18
CDs	Camptothecin	CDs	-	532 nm (1.12W/cm^2)	10 min	Chemo-PDT	19
Fe-TCPP	Tirapazamine	Porphyrin	-	660 nm (1 W/cm^2)	10 min	Ferroptosis, Chemo-PDT	20
ZnQ self-assembled NPs	Quercetin	Ce6	19.03	660 nm (60 mW/cm^2)	5 min	Chemo-PDT	This Work

References

1. M. J. Abraham, T. Murtola, R. Schulz, S. Páll, J. C. Smith, B. Hess and E. Lindahl, *SoftwareX*, 2015, **1–2**, 19–25.
2. J. Wang, R. M. Wolf, J. W. Caldwell, P. A. Kollman and D. A. Case, *Journal of Computational Chemistry*, 2004, **25**, 1157–1174.
3. A. Jakalian, D. B. Jack and C. I. Bayly, *Journal of Computational Chemistry*, 2002, **23**, 1623–1641.
4. J. Wang, W. Wang, P. A. Kollman and D. A. Case, *Journal of Molecular Graphics and Modelling*, 2006, **25**, 247–260.

5. D. A. Case, H. M. Aktulga, K. Belfon, I. Y. Ben-Shalom and P. A. Kollman, Amber 2023, *University of California, San Francisco*.
6. P. Li, L. F. Song and K. M. Jr. Merz, *J. Phys. Chem. B*, 2015, **119**, 883–895.
7. L. Martínez, R. Andrade, E. G. Birgin and J. M. Martínez, *Journal of Computational Chemistry*, 2009, **30**, 2157–2164.
8. E. J. Haug, J. S. Arora, and K. Matsui, *Journal of Optimization Theory and Applications*, 1976, **19**, 401-424.
9. J. R. Shewchuk, An introduction to the conjugate gradient method without the agonizing pain, 1994.
10. G. Bussi, D. Donadio and M. Parrinello, *The Journal of Chemical Physics*, 2007, **126**, 014101.
11. D. Bertsimas and J. Tsitsiklis, *Statistical Science*, 1993, **8**, 10–15.
12. H. J. C. Berendsen, J. P. M. Postma, W. F. van Gunsteren, A. DiNola and J. R. Haak, *The Journal of Chemical Physics*, 1984, **81**, 3684–3690.
13. U. Essmann, L. Perera, M. L. Berkowitz, T. Darden, H. Lee and L. G. Pedersen, A smooth particle mesh Ewald method, *The Journal of Chemical Physics*, 1995, **103**, 8577–8593.
14. B. Hess, H. Bekker, H. J. C. Berendsen and J. G. E. M. Fraaije, LINCS: A linear constraint solver for molecular simulations, *J. Comput. Chem.*, 1997, **18**, 1463–1472.
15. W. L. Jia, B. Jin, W. J. Xu, S. W. Liu, X. Y. Mao, H. Peng and Y. W. Zhang, *ACS Appl. Mater. Interfaces*, 2023, **15**, 50069–50082.
16. X. Han, Y. Li, Y. Zhou, Z. Song, Y. Deng, J. Qin, and Z. Jiang, *Materials & Design*, 2021, **204**, 109646.
17. Y. Zhou, C. Chang, Z. Liu, Q. Zhao, Q. Xu, C. Li, Y. Chen, Y. Zhang, and B. Lu, *Langmuir*, 2021, **37**, 2619-2628.

18. Q. Zhou, F. Mohammed, Y. Wang, J. Wang, N. Lu, J. Li, and Z. Ge, *Journal of Controlled Release*, 2021, **339**, 130-142.
19. G. Getachew, C. H. Hsiao, A. Wibrianto, A. S. Rasal, W. B. Direrssa, C.C. Huang, N. V. Rao, J. H. Chen, and J. Y. Chang, *Journal of Colloid and Interface Science*, 2023, **633**, 396-410.
20. W. L. Pan, Y. Tan, W. Meng, N. H. Huang, Y. B. Zhao, Z. Q. Yu, Z. Huang, W. H. Zhang, B. Sun, and J. X. Chen, *Biomaterials*, 2022, **283**, 121449.